Arch. Metall. Mater. **70** (2025), 2, 869-878

DOI: https://doi.org/10.24425/amm.2025.153488

R. ARIVUMANI[1], C. RAMKUMAR[1*], D. RAJASEKARAN[1], M. PALANISAMY[1], J. SRIDHARANIDHARAN[1], N. DHANARAJ[1], S. DEENADHAYALAN[1]

PROCESSING OF CERAMIC MATRIX COMPOSITES BY RMI TECHNIQUE AND CHARACTERIZATION OF THE (Al, Si, B_4C) COMPONENTS OF COMPOSITES

To attain the goal of receiving the well toughened ceramic matrix composite material for radioactive jackets to protect from nuclear radioactivity for commercial and defense applications. This research task is initiated to prepare the composites by preparing the Al-Si alloy at different propositions and infiltrate the alloy into the B_4C pellets at different temperatures. This task dealt with the methodology of reactive melt infiltration (RMI) technique and processing of ceramic matrix composites in lightweight. Moreover, it registered the phenomenon and factors influencing the infiltration process and characterization of constituents of the ceramic matrix infiltrated composites. Fine particles of 10 μm boron carbide powder (B_4C) was characterized by determining the free carbon content and thermal behavior experiments. By the addition of binder, the densification of porous B_4C green preforms and its pressing efficiency were analyzed. Four sets of Si-Al alloys were produced with various combinations and smelting parameters; and were investigated its property through XRD/EDS tests and SEM images. Nominal 50% porosity B_4C preforms were infiltrated by various proportions of hypereutectic Si-Al alloys at various batches through pressureless reactive melt infiltration process under inert argon atmosphere with different infiltration temperatures and infiltration duration. The poor infiltration, partial infiltration, changes in physical aspect, wetting phenomena were also discussed.

Keywords: Reactive melt infiltration; Wetting; Ceramic matrix composite; Boron carbide; Al-Si alloy

1. Introduction

There is a requirement and need to find more efficient and cost-effective processing processes and to include them in industrial patterns since a few ceramic metal composites perform a crucial role in the modern industry due to the increased benefits of excellent combinations of their features and qualities. This work, which is related to the other findings of the research team [1], aims to improve knowledge of novel composites by gathering information that can be used to build cost-effective design processes and processing techniques for attaining the best integration of ceramic and metal properties in reliable, lightweight composites.

Early on, the idea of using melt infiltration as a substitute method to create metal-ceramic and thick ceramic-matrix composites was put out [2-4]. The capillary forces created by soaking liquid into the pores of the fine-grain ceramic matrix would help to break the gravitational forces on the melt, which is an extremely important advantage [5]. When there are no interactions between the porous matrix and the melt, the rate of melt infiltration is determined and resolved by viscous flow, which is dependent on the viscosity of the melt, the porosity, the morphology of the porous bed, and the angle of wetting [3]. Darcy's law [6] normally governs viscous flow, and the sessile drop technique [7] is most frequently used to determine wettability. The techniques of capillary flow into packed beds are examined to consider meniscus effects to be substantial [8]. The desired shape is originally created in the reactive melt infiltration (RMI) process by creating the porous preforms. Contrarily, in non-wetting systems like aluminum-alumina, external pressure is necessary to force the infiltrate melt liquid into the open pores of the preforms [9]. This is because, in wetting systems like silicon and carbon, capillary forces and wetting contribute as driving factors of spontaneous RMI. The other advantages of RMI are preform conservation and near-net shape fabrication, which results in minimal or no post-process machining. RMI emphasizes near-net shape manufacture, which results in minimal or no post-process machining, as well as benefits such as the preservation of preform integrity in non-reacting systems, low material costs, time and cost efficiency, and speedy processing [10,11].

[1] DEPARTMENT OF MECHANICAL ENGINEERING, KIT-KALAIGNARKARUNANIDHI INSTITUTE OF TECHNOLOGY, COIMBATORE, 641402, INDIA

* Corresponding author: cmramkumar90@gmail.com

Al-Si alloy is lighter overall because silicon has a low density (2.34 gcm^{-3}) than aluminium. The several morphologies created by silicon inclusions in aluminum-silicon alloys include primary, compact, large precipitates hyper eutectic alloys, and branching plates of aluminum-silicon eutectic [12,13]. The composition of the melt, the rate of solidification, and the temperature gradient at the solid-liquid interface are a few of the parameters that control solidification and affect the mechanical and structural characteristics of the alloy [14]. According to Zhang et al.'s demonstration of low-density aluminum-silicon alloys with reactive boron carbide infiltration, it is feasible to manufacture boron carbide composites at affordable cost [15].

Powdered silicon, boron carbide, and pure forms of aluminium serve as the main components of this research study. According to research by Hayun et al., the inclusion of aluminium in the boron carbide-silicon system considerably increases the transition of initial boron carbide particles into a newly formed quaternary carbide phase and kinetics of rim-region growth. In the graphite furnace, this work was accomplished with the aid of alumina components. One of the sources for the inclusion of aluminium in composites was the infiltration of liquid silicon into B_4C preforms under vacuum at a temperature of 1753 K [16]. Toptan et al. described the inadequate wetting of boron carbide particles by liquid aluminium [17], which was resolved by Wu et al. [1].

2. Design procedure

The used raw materials were aluminum powder of 99.7% purity (ABCR GmbH & Co., CAS# 7429-90-5, lot#143946-11), powder of silicon about 99% pure (Emerk, Germany – 12497.0250, 201N628697), and 10μm average particle-sized boron carbide powder (EMS#50510-10, lot#BC80A22#36).

2.1. Testing and Preparation of B_4C Preforms

The preforms were made using B_4C powder with an average grain size of 10 μm and a density of 2.52 g/cm^3. In order to determine the quantity of graphite in this powder using the X-ray diffraction (DRX) method, a second batch of boron carbide powder (Electron Microscopy Sciences, EMS#50510-18, lot#BC50A25#08) was used. This powder had the lowest carbon content and an average particle size of 18 μm. The two powders were prepared and sent to X-ray diffraction in the following combinations: 75%, 50%, and 25% of each of the two powders, by weight. In order to understand the thermal behavior of the 10 μm B_4C powder, simultaneously, thermogravimetric analysis (TG) test and differential thermal analysis (DTA) test were carried out at temperatures of 800°C in the air where a mass of 29.2 g was consumed. Thermogravimetric analysis (TG) and differential thermal analysis (DTA) tests were conducted concurrently at temperatures of 800°C in the air with a mass of 29.2 g in order to comprehend the thermal behavior of the 10 μm B_4C powder.

In order to compress the boron carbide into cylindrical pellets with a 20 mm diameter and 7.5 mm height, the relative density was projected to be around 50% [1]. As a pressing aid, polyvinyl alcohol (PVA) solution of 4.0 wt.% was added to the dry B_4C powder (10 μm average particle size). By adding PVA as a binder and compressing the B_4C cylindrical pellets in uniaxial pressing (Carver Laboratory Press, uniaxial pressing with a capacity of 5 tonnes) at 60 MPa, then isostatic pressing (Autoclave Engineers, Penna USA) at 196 MPa, it was feasible to make cylindrical pellets with a nominal 50% relative density.

2.2. Preparation and Melting of Aluminium-Silicon Alloys

Four batches of aluminum-silicon alloys were created using the fusion process; the first two batches were created at 1000°C with silicon proportions of 25 and 35 wt.% using a resistance-heated graphite furnace at 50 kPa pressure in an inert atmosphere of argon gas, with heating rates of 20°C/min to 900°C, holds of 60 minutes, and with the same heating rates to 1000°C, followed by continuous cooling at a constant cooling rate of 50°C/min. Following this identical process, batches (3) and (4) were completed with a nominal silicon content of 25 wt.%, and the smelting was done twice.

For the reactive melt infiltration in the graphite furnace at 50 kPa pressure of argon gas environment, the prepared aluminum-silicon alloy was compressed as cylindrical shapes and retained on the top face of boron carbide porous preforms in intended estimated quantities. The infiltration of as-pressed preforms was carried out in several batches with an infiltration time of 5 minutes at the high-temperature range of 1100°C, 1200°C, or 1300°C. The density of infiltrating composites was determined using the Archimedes technique in water.

3. Results and discussion

Prior to discussing the results of reactive melt infiltration of boron carbide preforms, it is important to first analyze the proportion and qualities of the B_4C powders as given, the quality of compaction of the boron carbide preforms, the smelting and quality of the aluminum-silicon alloy, and the consequences and causes of infiltration processes. With the aid of photographs and interpretive methods, several non-infiltrations, partial-infiltrations, or poor infiltrations of the formed composites are also explored.

3.1. Characterization of B_4C Powder and Porous Preform

By considering the important characteristics for fine particles, distribution of size, and deagglomeration, this boron carbide with a mean particle size of 10 μm was chosen. This powder also

recognizes the rate of reactive melt infiltration, the efficiency of pressing packing, and the mechanical characteristics. The resultant infiltrated composites would have improved fracture toughness with a minimum of 5 wt.% free carbon and a mean grain diameter of 10 µm [18]. Since an internal standard in XRD, a coarser 18 µm average particle size of almost carbon-free boron carbide powder was used in this characterization. Weight loss caused by carbon in the air combustion was also used to calculate the free carbon content of 10 µm B_4C powder.

3.2. Content of the B_4C powder in terms of free carbon

The chemical analysis to determine the liberated carbon ratio of boron carbide material using EDS spectrometry with SEM may produce a misleading result owing to the weak atomic numbers present in the boron and carbon elements. SEM/EDS may rarely find the boron. According to XRD analysis of the given 10 µm boron carbide powder, Fig. 1(a) depicts the free carbon as graphite. The crystalline graphite was identified, and the amount of free carbon was derived by comparing the intensities of prominent XRD peaks from the graphite and boron carbide phases.

The XRD spectra of the 10 µm and 18 µm sized B_4C powders are shown in Fig. 1(b). Additionally, combinations of 10 µm B_4C powder with 75 wt.%, 50 wt.%, and 25 wt.% of 18 µm B_4C are displayed. The predominant peak of boron carbide is recorded at 38º (2θ angle) in the XRD spectra of the as-supplied 18 µm and 10 µm boron carbide powders. The occurrence of 2H graphite peaks at the 10 µm boron carbide powder's 2θ – 26° and 27° angles was the distinguishing difference.

TABLE 1 shows the matching intensity ratio values (2H graphite 2θ – 26 XRD peak) presented as a percentage of the intensity of the top position B_4C (2θ – 38 XRD) phase and their mixed ratios in the designed weight proportions. The combination of two separate boron carbide powders with varying grain sizes causes a slight variation in the intensity ratio of the carbon to boron carbide (C/B_4C) of the principal XRD peaks. In 10 µm sized boron carbide material, the intensity proportion of carbon/boron carbide of the primary XRD peak tip increases by around 16%, as shown in TABLE 1, indicating a growth in free carbon content. These quantifications do not take into consideration the difference in the mass absorption rate of the radiation among both states. A steady factor to the slope of the linear relationship of the examined XRD peak intensity of proportion was followed in order to fix the ratio of the boron carbide phase in the taken material. And, it is possible to determine the graphite (carbon) composition in 10 µm boron carbide powder with greater accuracy through this technique.

TABLE 1

Relative intensity of the 2H graphite of as-received powders in different proposition

Tests	10 µm (particle sized B_4C Powder)				18 µm
	100 wt.% of the B_4C	75 wt.% of the B_4C	50 wt.% of the B_4C	25 wt.% of the B_4C	100 wt.% of the B_4C
1	15.5	12.8	11.4	5.4	No Peaks Identified
2	16.3	10.9	8.3	4.2	

The maximum strength composition of C/B_4C for the 25 wt.% 10 µm sized boron carbide combination of powders has a significant relative error and a low accuracy. In the computation of the quantitative XRD technique that was provided, this value was not added. According to the numbers on each row in TABLE 1, XB = 0.93 and XB = 0.92 are the results of the proportion between the predicted estimates of the variable and the inclination of correlation yields XB = 0.93 and XB = 0.92 as findings. The 10 µm B_4C powder's free carbon content corresponds to values which were nearer to XC ≈ 8 wt.%.

3.1.1. Thermal analysis of the B_4C powders

Figs. 2(a) and 2(b) depict the simultaneous differential thermal analysis (DTA) and thermogravimetric (TG) for both

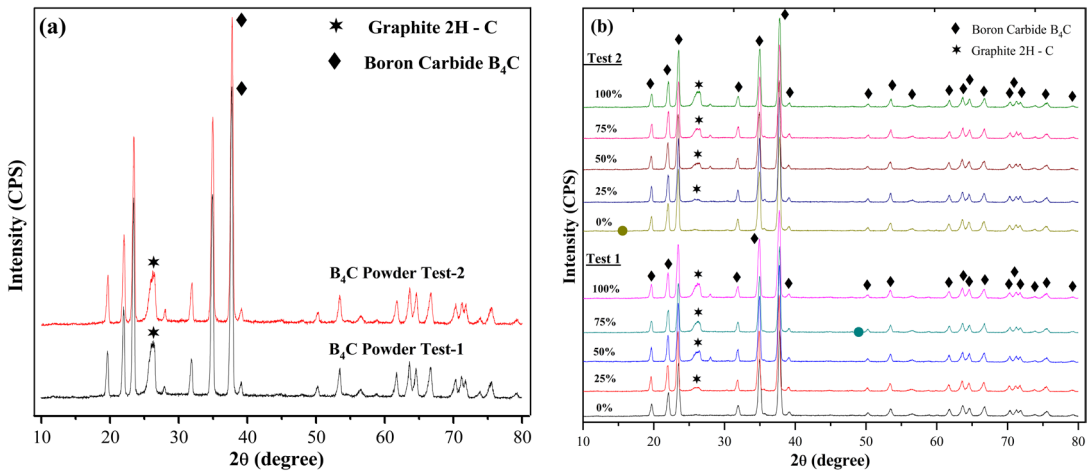

Fig. 1. Crystalline phases through X-ray diffraction spectra: (a) 10 µm B_4C powder as detected in two separated XRD tests, (b) as-supplied 10 µm and 18 µm B_4C powders and their mixtures; results of two independent tests

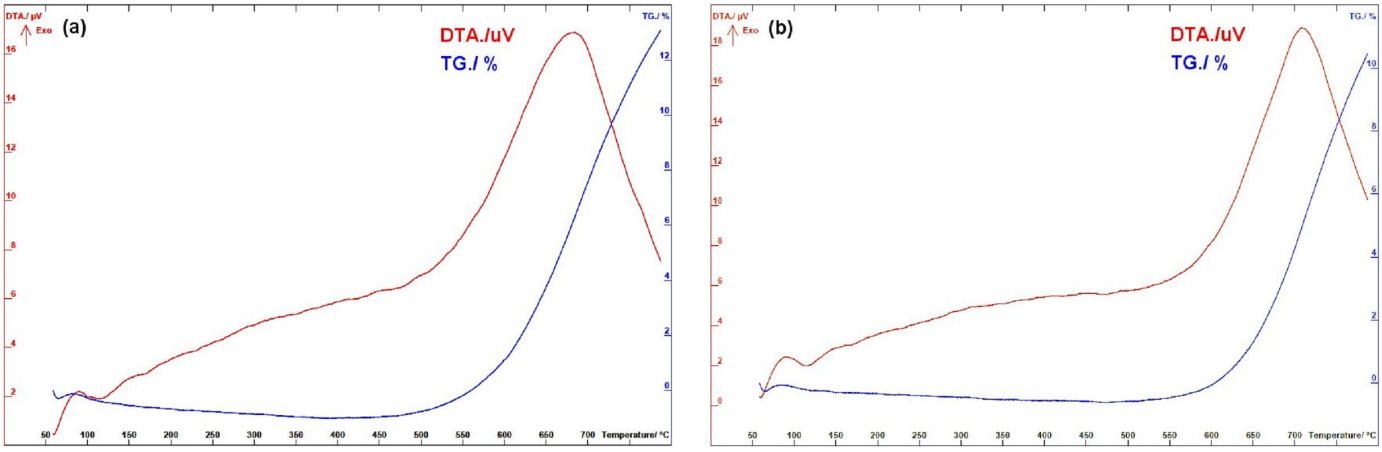

Fig. 2. DTA/TG examination in air: (a) 10 µm B_4C powder, (b) 18 µm B_4C powder

18 µm and 10 µm sized boron carbide (B_4C) powders, which were carried out in air at heating temperatures up to 800°C. Under 800°C, boron carbide begins to oxidize in the presence of B_2O_3 [19-22]. Owing to the fact that the temperatures for oxidation and combustion of the boron carbide particles exactly coincide, it is impossible to quantify how much weight is lost from the burning of free carbon components solely.

In Fig. 2(a), the 10 µm boron carbide powder exhibits a prominent exothermic peak at approximately 680°C, and the burning of free carbon and the oxidation of boron carbide both cause the weight loss shown in the thermogravimetric (TG) graph. If the free carbon is made up of graphite inclusions in dense aggregates of granules either held within boron carbide grains, the overlap of the two reactions will be more obvious. Fig. 2(b) exhibits a similar exothermic peak of the 18 µm boron carbide powder, progresses to a temperature of over 700°C, and observes that the weight loss is below the comparable level with the lesser carbon content. It also reveals the coarser sizes of boron carbide particles. Boron carbide particles undergo net oxidation in air at 800°C [19-21, 23].

The earliest onset of the exothermic response for the 10 µm boron carbide powder in Fig. 2(a) was compared to that for the 18 µm boron carbide powder in Fig. 2(b), yielding the indicative of the existence of graphite; and of smaller diameter grains of boron carbide powder correlating to Fig. 2(a).

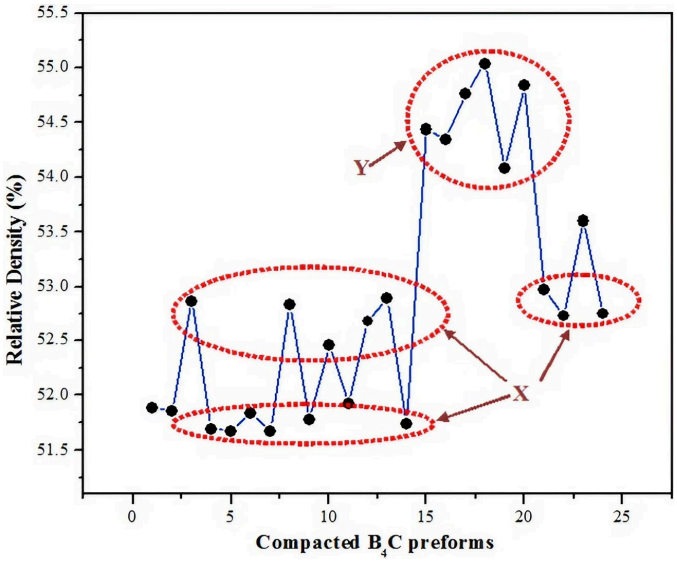

Fig. 3. Values of relative density of isostatic compacted B_4C preforms evaluated to regulate the activity

3.1.2. B_4C powder pressing effectiveness

The preform was prepared in accordance with the design technique. As seen in Fig. 3 and TABLE 2, the computed green density values of 24 compacted preforms fall between

TABLE 2

Samples of isostatic pressed B_4C preform with its corrected green density, relative density and the PVA solution added for binding

Samples		1	2	3*	4	5*	6	7	8	9	10	11	12
Corrected green density	(g/cm^3)	1.31	1.31	1.33	1.30	1.30	1.31	1.30	1.33	1.30	1.32	1.31	1.33
Relative density	%	51.9	51.9	52.9	51.7	51.7	51.8	51.7	52.8	51.8	52.5	51.9	52.7
PVA solution added	wt. %	3		4.5								3.5	4.5

Samples		13*	14*	15	16*	17*	18	19*	20	21	22	23	24
Corrected green density	(g/cm^3)	1.33	1.33	1.30	1.37	1.37	1.38	1.39	1.36	1.38	1.34	1.33	1.35
Relative density	%	52.9	51.7	54.4	54.3	54.8	55.0	54.1	54.8	53.0	52.7	53.6	52.8
PVA solution added	wt.%	4.5		5							4	4.5	4
PVA solution added	wt.%	3		4.5								3.5	4.5

* successfully pressed specimens

1.25 g/cm^3 to 1.46 g/cm^3. The relevant relative density values have been depicted in Fig. 3. When comparing isostatic pressing to the initial uniaxial pressing, green density is enhanced by around 6%. Additionally, isostatic pressing offers a constant shape for the preform. Good binding is ensured by the initial use of PVA.

Early on in the infiltration process, heating completely evaporated all of the water in the binder. The mean green density of isostatically pressed preforms is 1.330±0.03 g/cm^3 (or 47.2%), while the porosity percentage for pure boron carbide is 2.52 g/cm^3. The green preform's pre-set densification value is around 50%, although the measured relative density is somehow greater than the pre-set. Some of the experimental variables that have contributed to the dispersion of green density values of preforms include the amount of additional binder, its regularity of distribution, degassing before the last phase of cold isostatic pressing, and maintained humidity. Preforms were manufactured in batches with various PVA solution concentrations to provide the best compacting performance. In Fig. 3, two sets of relative density values for the preforms are shown; X denotes the addition of 4 to 4.5 wt.% of PVA solution, while Y denotes the use of 5.0 wt.% of PVA solution in the preforms.

3.2. Characterization of the Al-Si Alloy

The structure of phases, constituent combination and composition, and mechanical characteristics of alloys are all significantly influenced by the solidification process. TABLE 3 lists the smelting circumstances, nominal aluminum and silicon concentrations, number of smelting, and the outcomes of SEM/EDS and XRD analyses for four batches. Following the melting, the nominal composition of the first fusion batch was close to the corresponding proportion. The latter two batches were smelted twice in an effort to obtain an alloy of substantially higher grade.

The XRD outcomes for the fusion batch are shown in Fig. 4, and the dendritic development of Al-35 wt.% Si alloy with star-shaped clusters of Si is shown in Fig. 5. With the help of quantitative measurements of the primary peaks of phases in DRX (2° = 28.5° for Si and 2° = 38.5° for Al), the weight fractions of silicon and aluminum in the fusion (Al-Si alloy) batches were determined and compared to the corresponding peak intensity ratios of standards made of silicon and aluminum powder mixtures. In this study, it is mostly due to a larger concentration of silicon and a rate of solidification occurring under superior cooling.

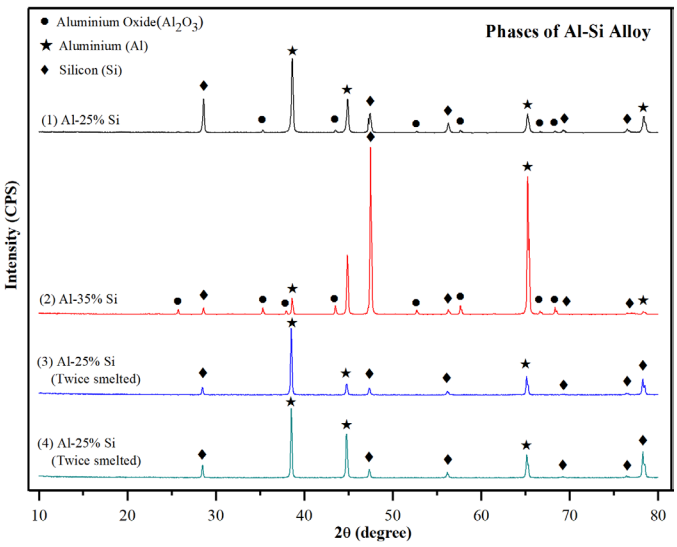

Fig. 4. Responses of four sets of Al-Si alloy smelting under X-Ray Diffraction

In their study on the precipitation of silicon in an alloy with an Al-30 wt.% Si content, Nikanorov et al. [14] describe a similar process in which the formation of dendrites resulted in silicon aggregates that resembled stars. While the 25 wt.% Si alloy does not exhibit any star or needle-like dendrites, the Al-35 wt.% Si alloy particles exhibit dendrite development as star-like agglomerates. The Fig. 6. shows the alloy of 23.8 wt.% Si content of batch (1), in which the growth of particles do not show any star or needle like dendrites.

For the range of composition of the present study the decrease of density of Al-Si alloy with the Si content is almost linear [24]. In the hypoeutectic Al-Si alloy, increasing of Si content improves the hardness of the alloy, whereas in the hypereutectic alloy (>12.7 wt.% Si) there is the opposite trend [24]. The Al-Si alloys of the present study are hypereutectic. As Si is taken out of the alloy during reactive melt infiltration of the B_4C ceramic preforms the composition of the metallic phase moves towards the eutectic composition and the yield stress and hardness of the metallic phase in the composite may increase. The composition of the melt, the temperature gradient at the solid-liquid interface and crystallization rate are major factors in solidification. The

TABLE 3

Quantitative DRX measurements and status of density of different Al-Si alloy batches

Batch / Set	Al-Si Nominal (wt.%)	Al-Si Measured (wt.%)				Density (g/cm^3)	
		XRD		EDS		Nominal	Calculated
		Al	Si	Al	Si		
1	25% Si	76.2	23.8	62.4	37.6	2.60	2.60
2	35% Si	70.0	30.0	52.0	48.0	2.56	2.58
3	25% Si*	83.0	17.0	71.0	29.0	2.60	2.63
4	25% Si*	78.0	22.0	73.1	26.9	2.60	2.61

* alloy smelted twice

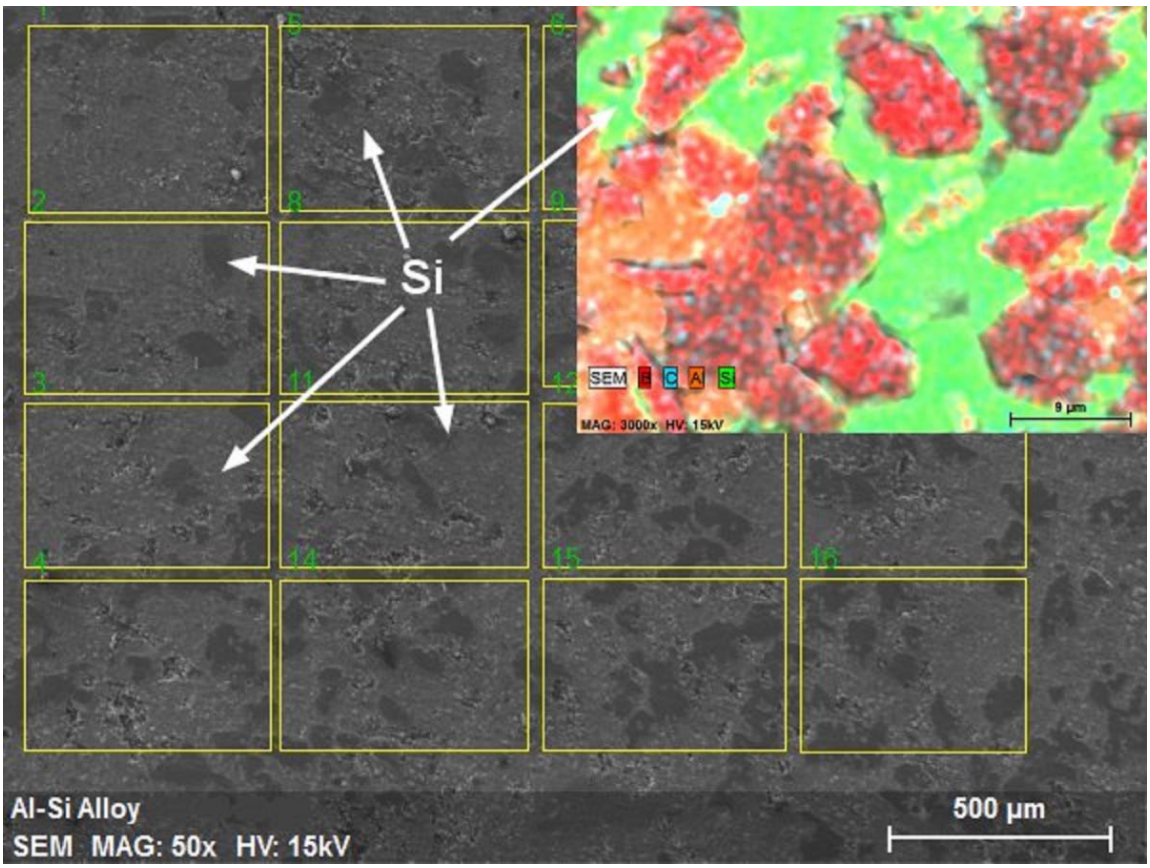

Fig. 5. Development of dendrites of silicon aggregates at Al-35 wt.% Si alloy

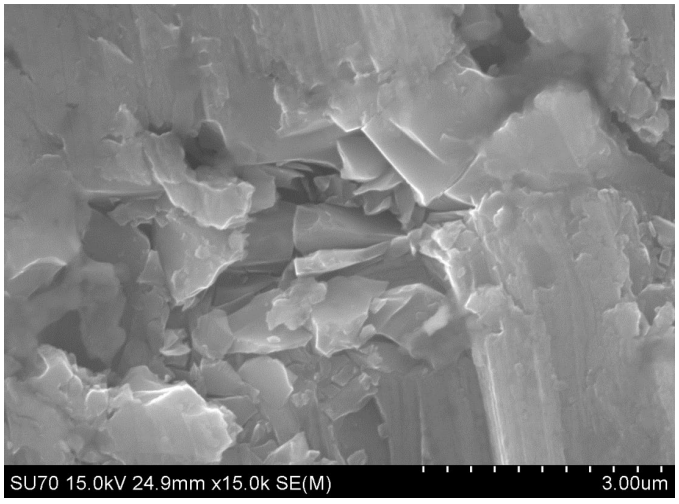

Fig. 6. Bulky dendrite formation in Al-25 wt.% Si alloy of fusion batch

simultaneous changes of these factors may lead to conflicting effects on the formation of the microstructure of the solidified alloy and its mechanical behaviour.

3.3. Aluminium – Silicon Reactive Melt Infiltration of B_4C

During infiltration and solidification processes, the aluminum-silicon alloy interacted with boron carbide components, creating new carbide phases. At the lowest temperatures, the infiltration length is a critical factor; it allows the metal to pass into the whole depth of the open-pored preform and protects the quantity of silicon in the alloy above the critical level of 12.6 wt.% silicon, which is required for the production of brittle aluminum carbide [21]. The capillary forces of surface tension have the ability to cause spontaneous infiltration. Early research [25] suggests that boron carbide reacts with liquid silicon, aluminum, and other metals in the pellet during the infiltration process. The spreading of metal has been studied on the polished surfaces of sintered boron carbide ceramic specimens. Nearly at 1200°C, liquid aluminum may spread freely over the flat surface of boron carbide at the velocity range from 1×10^{-4} m/s to 8×10^{-4} m/s [25]. Additionally, the hypereutectic aluminum alloy develops at a velocity that makes it possible to infiltrate a layer of 15 mm thickness in less than three minutes.

The same study also indicates that the spreading of aluminum was irregular and abruptly decreased from four to five minutes due to the emergence of recent phases, which reduced the driving power for the liquid aluminum's flow on the boron carbide to nearly zero. In addition, after three minutes, the angle of contact of molten aluminum had decreased from 92° to 28°, which caused viscous flow to impede the aluminum's progress. According to Panasyuk et al., after the first three minutes with the rapid non-linear reduction to time, the velocity of spreading of molten silicon over the boron carbide surface will become steady and close to nil [25]. The infiltration of porous boron carbide

preform is regulated by either the reaction rate or the imbibition velocity (controlled by absolute viscosity) of the molten materials and pressure of curvature. The liquid within the pore channels generates the meniscus's concave curvature under pressure.

As depicted in Fig. 7, the liquid used to infiltrate the boron carbide moved from the top section of the pellet (on the right) to the bottom section (on the left) of the flaw. This route of the melting aluminum-silicon alloy is shown. It may be seen spreading through a narrow split in the porous material in Fig. 7. Simultaneously with the flaw being filled up, the composite matrix next to it reached complete infiltration. Fig. 7 indicates the path of the progressing molten aluminum-silicon alloy on a thin flaw where at the time of the boron carbide infiltration, the fluid traveled down the pellet from the upper portion to the lower side. Fig. 7 shows the alloy distributing across a small defect in the porous substrate. The composite matrix in the vicinity of the flaw also became fully infiltrated simultaneously the flaw went filled in.

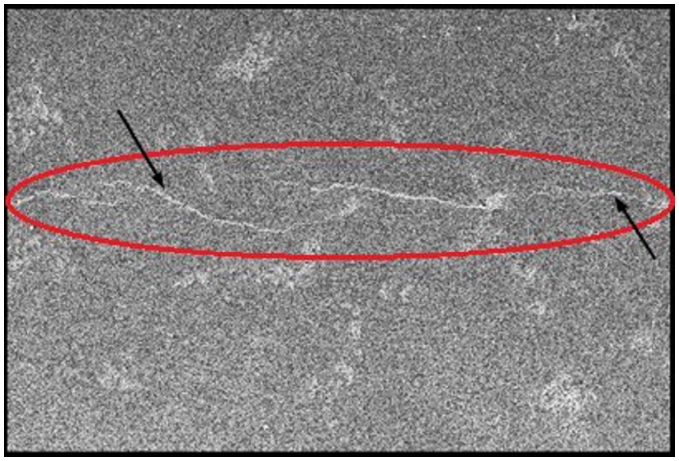

Fig. 7. Sectioned projection of a RMI B_4C ceramic matrix composite (*arrow mark indicates the top side, is the beginning of the direction of infiltration*)

TABLE 4 lists the conditions that were used to prepare the composites as well as the final densities and relative densities of composites and the corrected relative densities (densification) of the preforms. The green bodies' densification exceeds the desired value of 50% relative density by 1.7% to 4.8%. However, it was unable to reduce the PVA solution from 4.5 wt.% to even 3.0 wt.% because the green body was affected at the time of handling, particularly during the cold isostatic pressing process.

TABLE 3 shows the actual density of the aluminum-silicon alloy, which was taken into consideration while determining the theoretical density. The nominal weight percentage of silicon in the aluminum-silicon combination is shown in TABLE 4. Although the composites I, III, and VII were made from varied ratios of aluminum-silicon alloy, different infiltration conditions, and various smelting procedures, they nevertheless had a density of 2.53 g/cm^3 or greater when measured, and their relative density was close to 99%. For this reason, those fully infiltrated composites were chosen for further study on their structure and mechanical properties.

3.4. Failure of the Melt Infiltration Process

Reactive infiltration flaws account for the remaining composites in TABLE 4 with lower relative densities. Some preforms did not completely infiltrate during the infiltration procedures due to poor wetting and oxidation concerns. Fig. 8 depicts the three pellets from the same infiltration batch that were run at 1300°C, with one perform that was not infiltrated, detected, while the other two pellets were fully infiltrated. The alumina plates were coated with an alumina slurry for easy removal following the infiltration. When reduced, this thin layer of alumina powder becomes a source of oxidative gases (CO/CO_2) once it has less interaction with the boron carbide itself or the carbon in the pellet. When evaluating the root causes of non-infiltrating activities, it was found that poor wetting and metal oxidation were the main issues. The presence of contaminants, such as moisture from the coating slurry, gases adsorbing on the ceramic surface particles, or from the sample, results in an aluminum sub-oxide layer, an aluminum oxide (Al_2O_3) layer surrounding the liquid aluminum, and a native silicon dioxide (SiO_2) layer that only covers silicon particle surfaces [26-28]. In these instances, it is frequently prohibited for the hot metallic matrix to make direct contact with the surfaces of every single grain [27].

After the formation of liquid-solid bonds, there is a crucial rearrangement step during the spreading phase where the liquid spreads out to wrap the solid surfaces. Factors influencing the process include the angle of the dihedral and solution infiltra-

TABLE 4

List of partial and complete infiltrated B_4C composites with various preparation parameters

Composites	Densification (%)	Nominal Si Content (%)	Densities of the Composites (g/cm^3)			Infiltration Parameters
			Theoretical	Measured	Relative	Calculated
I*	52.9	25	2.57	2.55	99.51	1300°C – 5 minutes
II	51.7			2.44	95.00	
III*	52.9	35	2.55	2.53	99.07	
IV	51.7			2.50	98.02	
V	54.3	25 (Twice Smelted)	2.58	2.51	97.51	
VI	54.8			2.51	97.47	
VII*	54.1			2.55	98.72	1200°C – 5 minutes

* completely infiltrated composites

Fig. 8. Results of RMI process accomplished under 1300°C (A) non-infiltrated preform of B_4C; (B) on top of preform remnants of the Si-Al alloy; (C) thin layer of aluminium oxide (D) aluminium oxide plate; (E) and (F) completely infiltrated composites

tion at the border of the grains. The majority of solids are often found to be easily wetted by low surface tension liquids with minimal contact angle, while poor wetting is typically observed with high surface tension liquids with significant contact angles.

Once the cohesiveness within liquid molecules is stronger than the adhesion of solid and liquid molecules, the liquid does not exhibit a tendency to moisten the solid at the atomic scale. In certain instances, the infiltration won't happen. There were some extremely small areas where the aluminum-silicon alloy underwent oxidation as a result of the operations. In alumina crucibles, the alloys were created. Despite the alloy smelting in an environment of inert gas, an oxide layer formed on its surface. Additionally, the emergence of a networked structure with precise pockets of smelted alloy was noted. The oxide layer was removed, the alloy was divided into smaller pieces, and then pressed as previously mentioned to promote greater wetting and early dispersion. Smaller oxide particles only remained within the alloy pieces.

3.5. Partial Melt Infiltration of B_4C Preforms

The variation in spreading speed along the alloy's porosity regions is what causes infiltration anomalies. It's possible that this is linked with chemical processes that happened in the specimen volume during infiltration or defects in the pellets. The variance in particle packing efficiency is brought on by the uneven loading during pressing and the internal friction of hard boron carbide particles. Internal flaws are brought on by delamination of compressed pellets.

Gases would be produced by the pyrolysis and degradation of polyvinyl alcohol (the binder). According to Figs. 9(a) and 9(b), it could take longer than planned to remove gaseous pollutants and residual water that remains in the compacted pellets' center volume. As a result, the holding period was later extended (from 15 to 30 minutes at 500°C) to reduce the chance of irregularities forming. Fig. 9(b) demonstrates the pattern for prolonged infiltrate activity at the end face of the pellet's center, which was noticed earlier [4]. This irregularity results from incomplete infiltration at the intended temperature for a prolonged duration.

In comparison to the viscosity of water at atmospheric ambient temperature, liquid aluminum has a lower dynamic viscosity in the 1000-1350°C temperature range, ranging from 0.6-0.8 mPa.s [29]. The presence of silicon in the pure aluminium improves the viscosity of the Si-Al alloy, since the purity of the aluminium affects the viscosity of it [30]. Once the temperature rises, the surface tension of the alloy drops and approaches that of pure aluminum. The molten aluminum's contact angle with the boron carbide surface must reveal the composition of the alloy and its almost complete temperature dependency [31].

Fig. 9(c) shows how the concave meniscus of molten aluminum-silicon alloy vanishes and how the rate of mobility of melt beneath surface tension stresses either ceases or has localized retardation, abandoning the apparent void less space. By accumulating binder and then removing it later during heating, binder masses experience differential internal shrinkage that results in the formation of cavities and pores surrounding them. When organic contaminants such as flakes of graphite or other contaminants are present in the powder that is delivered, similar voids can occur in the internal structure of the pellets. Due to internal faults on planes and on the surfaces of pores, it is discovered that regular particle coordination of boron carbide as well as packing fraction has terminated.

4. Conclusion

Four batches of Al-Si alloy were produced using a smelting process with nominal silicon proportions of 25 wt.% and 35 wt.% in a graphite furnace. Two batches were smelted twice

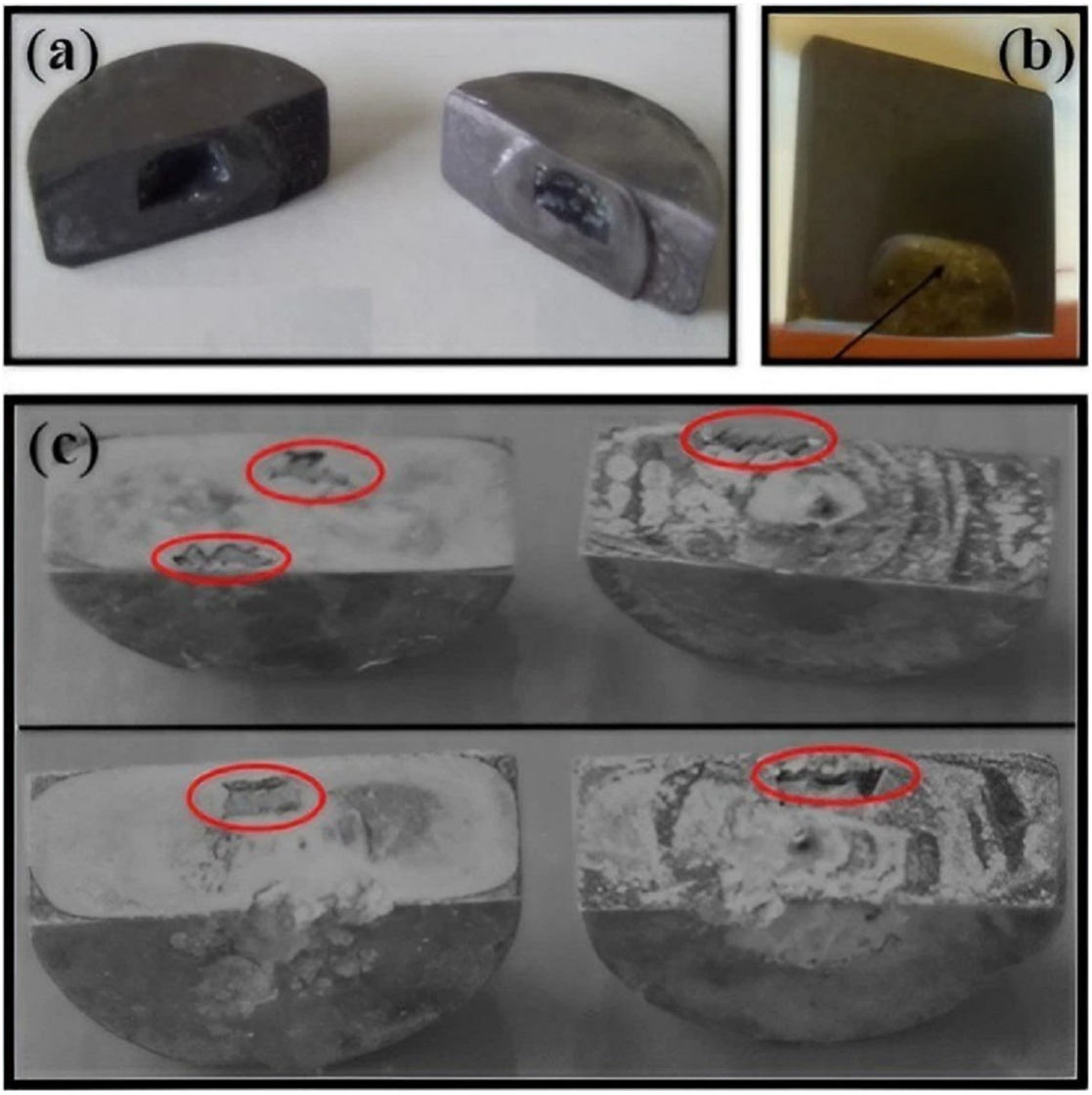

Fig. 9. Cross sectioned view of composites with partial infiltration condition, (a) volume that has not been invaded in the middle (Composite II), (b) a composite with a depression surface of a molten Si-Al alloy due to the retarded surface tension during infiltration, (c) Composites V (top) and VI (bottom) with on-infiltrated volumes and irregularly shaped flaws

for homogeneity. A 10 μm boron carbide powder, with graphite impurity and approximately 8% carbon content, was used. Porous preforms with relative densities between 51.7-54.8% were produced via unidirectional compression and cold isostatic pressing.

- Composites were produced by infiltrating hypereutectic Si-Al alloys into B_4C preforms using the reactive metal infiltration (RMI) method.
- Complete infiltration of 7.5 mm high cylindrical boron carbide preforms was achieved with quick heating cycles at 20°C/min and 5 minutes of isothermal holding at 1200°C and 1300°C.
- Infiltration was not successful at 1100°C.
- Some preforms experienced partial or no infiltration due to oxidation and inadequate wetting issues.
- The presence of gaseous oxygen constituents affected the infiltration process. Stability and consistency were improved by flushing the furnace atmosphere with argon gas before infiltration.

Based on the outcomes of this study Introducing wetting dopants during the formulation of aluminium-silicon alloy can enhance infiltration dynamics and reduce susceptibility to oxygen pollution. Considering the results this material can be further developed for utilizing it as the layer of radioactive jackets. Achieving higher green density of B_4C preforms through efficient forming techniques and optimized particle size distribution can lead to better quality composites.

REFERENCES

[1] H. Wu, S. Zhang, M. Gao, D. Zhu, Y. Pan, Y. Liu, H. Pan, F.J. Oliveira, J.M. Vieira, Microstructure and mechanical properties of multi-carbides/(Al, Si) composites derived from porous B4C preforms by reactive melt infiltration. Mat. Sci. Eng. A (551), 200-208 (2012).
DOI: https://doi.org/10.1016/j.msea.2012.05.008

[2] J. Chadam, D. Hoff, E. Merino, P. Ortoleva, A. Sen, Reactive infiltration instabilities. J. Appl. Math. **3** (36), 207-221 (1986). DOI: https://doi.org/10.1093/imamat/36.3.207

[3] W.B. Hillig, Melt infiltration approach to ceramic matrix composites. J. Am. Ceram. Soc. **2** (71), C-96-C-99 (1988). DOI: https://doi.org/10.1111/j.1151-2916.1988.tb05840.x

[4] C. Toy, W.D. Scott, Ceramic-metal composite produced by melt infiltration. J. Am. Ceram. Soc. **1** (73), 97-101 (1990). DOI: https://doi.org/10.1111/j.1151-2916.1990.tb05097.x

[5] P. Yi, S. Kewei, Preparation of TiC/Ni3Al composites by upward melt infiltration. J. Mater. Sci. Technol. **04** (16), 387 (2000).

[6] S. Whitaker, Flow in porous media I: A theoretical derivation of Darcy's law. Transport. Porous. Med. **1**, 3-25 (1986). DOI: https://doi.org/10.1007/BF01036523

[7] T. Young, III. An essay on the cohesion of fluids. Philosophical Transactions of the Royal Society of London **95**, 65-87 (1805). DOI: http://dx.doi.org/10.1098/rstl.1805.0005

[8] J.W. Gibbs, The Collected Works of J. Willard Gibbs...: Thermodynamics, Longmans, Green and Company, 1928.

[9] A. Mortensen, J.A. Cornie, M.C. Flemings, Solidification processing of metal-matrix composites. Jom-J. Min. Met. Mat. S **2** (40), 12-19 (1988). DOI: https://doi.org/10.1007/BF03258826

[10] M. Gupta, S. Ling, Microstructure and mechanical properties of hypo/hyper-eutectic Al–Si alloys synthesized using a near-net shape forming technique. J. Alloy. Compd. **1-2** (287), 284-294 (1999). DOI: https://doi.org/10.1016/S0925-8388(99)00062-6

[11] K. Schwetz, Silicon carbide based hard materials. Handbook of ceramic hard materials, 683-748 (2000).

[12] J. Davis, J. Davis, ASM International Handbook Committee: Aluminum and aluminum alloys. ASM specialty handbook, Materials Park, OH, ASM International, (33), (1993).

[13] S.-Z. Lu, A. Hellawell, Modification of Al-Si alloys: Microstructure, thermal analysis, and mechanisms. Jom-J. Min. Met. Mat. S **47**, 38-40 (1995). DOI: https://doi.org/10.1007/BF03221405

[14] S. Nikanorov, M. Volkov, V. Gurin, Y.A. Burenkov, L. Derkachenko, B. Kardashev, L. Regel, W. Wilcox, Structural and mechanical properties of Al–Si alloys obtained by fast cooling of a levitated melt. Mat. Sci. Eng. A.-Struc. **1-2** (390), 63-69 (2005). DOI: https://doi.org/10.1016/j.msea.2004.07.037

[15] W. Zhang, S. Yamashita, H. Kita, Progress in pressureless sintering of boron carbide ceramics – a review. Adv. Appl .Ceram. **4** (118), 222-239 (2019). DOI: https://doi.org/10.1080/17436753.2019.1574285

[16] S. Hayun, A. Weizmann, H. Dilman, M. Dariel, N. Frage, Rim region growth and its composition in reaction bonded boron carbide composites with core-rim structure. In: J. Phys. Conf. Ser. 2009. IOP Publishing.

[17] F. Toptan, A. Kilicarslan, I. Kerti, The effect of Ti addition on the properties of Al-B4C interface: a microstructural study. In: Mater. Sci. Forum. 2010. Trans. Tech. Publ.

[18] K.A. Schwetz, L.S. Sigl, L. Pfau, Mechanical properties of injection molded B4C–C ceramics. J. Solid. State. Chem. **1** (133), 68-76 (1997). DOI: https://doi.org/10.1006/jssc.1997.7316

[19] D. Emin, T. Aselage, A. Switendick, B. Morosin, C. Beckel, Boron-rich solids. 1991, American Inst. of Physics, New York, NY (USA).

[20] L.M. Litz, R. Mercuri, Oxidation of boron carbide by air, water, and air-water mixtures at elevated temperatures. J. Electrochem. Soc. **8** (110), 921 (1963). DOI: https://doi.org/10.1149/1.2425901

[21] M. Heuberger, R. Telle, G. Petzow, Modification of ceramic powders by ion beam treatment. Powder. Metall. **2** (35), 125-132 (1992). DOI: https://doi.org/10.1179/pom.1992.35.2.125

[22] A. Rahimi, M. Shamanian, J.A. Szpunar, Effect of pulsed current frequency on microstructure and mechanical properties of Gas-Tungsten-Arc-Welded Joints of UNS R30155. J. Mater. Eng. Perform. **29**, 2635-2647 (2020). DOI: https://doi.org/10.1007/s11665-020-04752-7

[23] M. Shamanian, A. Rahimi, J.A. Szpunar, Characterization of microstructure and texture across N155 superalloy weldment joint with austenitic filler Metal. J. Mater. Eng. Perform. **29**, 1964-1973 (2020). DOI: https://doi.org/10.1007/s11665-020-04707-y

[24] A. Panasyuk, V. Oreshkin, V. Maslennikova, Kinetics of the reactions of boron carbide with liquid aluminum, silicon, nickel, and iron. Sov. Powder. Metall. **18**, 487-490 (1979). DOI: https://doi.org/10.1007/BF00797254

[25] A. Ravanan, J.M. Vieira, B. Almeida, C. Ramkumar, F.J. Oliveira, A. Lopes, H. Wu, Processing and Mechanical properties of dual-carbide (B4C, SiC), dual-metallic phases (Al, Si) infiltrated composites. Mater. Today-Proc. **16**, 374-383 (2019). DOI: https://doi.org/10.1016/j.matpr.2019.05.104

[26] H. Ribes, R. Da Silva, M. Suery, T. Bretheau, Effect of interfacial oxide layer in Al–SiC particle composites on bond strength and mechanical behaviour. Mater. Sci. Tech. Ser. **7** (6), 621-628 (1990). DOI: https://doi.org/10.1179/mst.1990.6.7.621

[27] A. Rahimi, M. Shamanian, M. Atapour, Effect of pulse current frequency on microstructure and hot corrosion behavior of tungsten inert gas-welded joints of N155 superalloy. J. Mater. Eng. Perform. **10** (30), 7494-7509 (2021). DOI: https://doi.org/10.1007/s11665-021-05878-y

[28] M.J. Assael, K. Kakosimos, R.M. Banish, J. Brillo, I. Egry, R. Brooks, P.N. Quested, K.C. Mills, A. Nagashima, Y. Sato, Reference data for the density and viscosity of liquid aluminum and liquid iron. J. Phys. Chem. Ref. Data **1** (35), 285-300 (2006). DOI: https://doi.org/10.1063/1.2149380

[29] A. Dinsdale, P. Quested, The viscosity of aluminium and its alloys – A review of data and models. J. Mater. Sci. **39**, 7221-7228 (2004). DOI: https://doi.org/10.1023/b:jmsc.0000048735.50256.96

[30] D.C. Halverson, A.J. Pyzik, I.A. Aksay, W.E. Snowden, Processing of boron carbide-aluminum composites. J. Am. Ceram. Soc. **5** (72), 775-780 (1989). DOI: https://doi.org/10.1111/j.1151-2916.1989.tb06216.x